JACS
JOURNAL OF THE AMERICAN CHEMICAL SOCIETY

Article

Boosting Enantioselectivity of Chiral Organocatalysts with Ultrathin 2D Metal–Organic Framework Nanosheets

Chunxia Tan, Kuiwei Yang, Jinqiao Dong, Yuhao Liu, Yan Liu, Jianwen Jiang, and Yong Cui

J. Am. Chem. Soc., **Just Accepted Manuscript** • DOI: 10.1021/jacs.9b07633 • Publication Date (Web): 13 Oct 2019

Just Accepted

is published by the American Chemical Society. 1155 Sixteenth Street N.W., Washington, DC 20036

Boosting Enantioselectivity of Chiral Organocatalysts with Ultrathin 2D Metal–Organic Framework Nanosheets

Chunxia Tan,[†] Kuiwei Yang,[‡] Jinqiao Dong,[†] Yuhao Liu,[†] Yan Liu,[*,†] Jianwen Jiang[*,‡] and Yong Cui[*,†]

[†]School of Chemistry and Chemical Engineering and State Key Laboratory of Metal Matrix Composites, Shanghai Jiao Tong University, Shanghai 200240, China

[‡]Department of Chemical and Biomolecular Engineering, National University of Singapore, 4 Engineering Drive 4, 117576 Singapore

Supporting Information

ABSTRACT: The development of methodologies for inducing and tailoring enantioselectivities of catalysts is an important issue in asymmetric catalysis. In this work, we demonstrate for the first time that chiral molecular catalysts can be boosted from completely non-selective to highly enantioselective when installed in nanostructured metal-organic frameworks (MOFs). Exfoliation of layered crystals is one of the most direct synthetic routes to unltrathin nanosheets, but its use in MOFs is limited by the availability of layered MOFs. We illustrate that layered MOFs can be designed using ligand-capped metal clusters and angular organic linkers. This leads to the synthesis of two 3D layered porous MOFs from Zn_4-*p*-*tert*-butylsulfonyl calix[4]arene and chiral angular 1,1'-binaphthol/-biphenol dicarboxylic acids, which can be ultrasonic exfoliated into one- and two-layer nanosheets. The obtained MOF materials are efficient catalysts for asymmetric cascade condensation and cyclization of 2-aminobenzamide and aldehydes to produce 2,3-dihyroquinazolinones. While both binaphthol and biphenol display no enantioselectivity, restriction of their freedom in the MOFs leads to 56-90% and 46-72% ee, respectively, which are increased to 72-94% and 64-82% ee after exposure to external surfaces of the flexible nanosheets. Moreover, the MOF crystals and nanosheets exhibit highly sensitive fluorescent enhancement in the presence of chiral amino alcohols with enantioselectivity factors being respectively increased up to 1.4 and 2.3 times of the values of the diols, allowing them to be utilized in chiral sensing. Therefore, the observed enantioselectivities increase in the order organocatalyst < MOF crystals < MOF nanosheets in both catalysis and sensing. This work not only provides a strategy to make 3D layered MOFs and their untrathin nanosheets, but also paves the way to utilize nanostructured MOFs to manipulate enantioselectivities of molecular catalysts.

INTRODUCTION

Because of the importance of chirality in pharmaceutical and biological chemistry, the development of methodologies for preparing and detecting enantiopure compounds is an important issue.[1] The use of chiral metal and organic complexes as homogeneous catalysts is a well-established and efficient strategy for the synthesis of optically active compounds.[2,3] Varying steric and electronic properties of catalysts have a significant effect on substrate activation and structures of transition states and intermediates, and have been widely used to control stereoselectivity in asymmetric catalysis.[4] In this work, a new method of manipulating enantioselectivities of molecular catalysts is presented. We demonstrate that nanostructured metal-organic frameworks (MOFs) can be used as a promising platform to induce and tailor enantioselectivitie of organocatalysts in both catalysis and sensing. Furthermore, this method can also facilitate separation and recycling of homogeneous catalysts. It should be noted that the multiplicity and intractability of the active sites in conventional chiral solids often complicate structure/performance-based control over regio- and stereoselectivity.[5]

MOFs are a highly versatile class of porous crystalline hybrid materials with many applications.[6] By taking advantage of their permanent porosity and tunable structures, MOFs provide a powerful platform to integrate chiral building blocks into robust structures for enantioselective processes.[7-11] A number of chiral MOF-based catalysts and sensors with modest to high enantioselectivity have been designed, including binol-, biphenol- and metallosalen-based MOFs.[9-11] In a relative few cases, enantioselectivity enhancement was observed relative to monomeric models due to confinement effects within the frameworks facilitating host-guest interactions and/or synergistic interactions with substrates.[9c,10b,11c] However, none of the materials yet reported is capable of inducing enantioselectivity from non-selective catalysts. By reducing one dimension of MOFs to single or few layers, 2D MOF nanosheets (MONs) have emerged as a new class of functional 2D materials.[12] Compared with the 3D MOF bulk crystals, the merits of combining more accessible active sites, super flexibility, faster diffusion, and improved host-guest affinity of substrates/products within 2D MONs make them ideal candidates as highly active catalysts[13] and sensors.[14] Nonetheless, chiral MONs remains a virgin land waiting for exploration,[15] and there is no report of MONs for enantioselective catalysis and sensing. Among various known methods for fabrication of MONs, exfoliation of 3D layered MOF crystals into their 2D constituents is one of the most direct approaches, in which various driving forces are used to break weak van der Waals interactions between the stacked layers.[16] Unfortunately, the types of 3D layered MOFs are still limited, preventing its wide use.[15,16a,17] This limitation represents a major challenge in preparing 2D MONs.[12f] To address this issue, here we illustrate a new strategy for preparing layered MOFs by using bulky hydrophobic ligand-capped metal clusters as building blocks. Such weak hydrophobic interactions between interlayers would benefit the fabrication of ultrathin 2D anisotropic MONs via ultrasonic liquid exfoliation.

Sulfonylcalix[4]arenes can react with metal ions to form a shuttlecock-like tetrametallic clusters, which are capable of serving as four-connected nodes to make discrete coordination

cages by treating with linear rigid organic linkers.[18] With the hydrophobic TBSC-capped Zn_4 clusters (H_4TBSC = *p*-*tert*-butylsulfonyl calix[4]arenes), we show that 3D porous layered MOFs can be synthesized from semi-rigid and angular organic linkers (Figure 1). The desired MOFs constructed from enantiopure 2,2'-dihydroxyl-1,1'-binol(biphenol)-3,3'-dicarboxylic acids can be easily ultrasonic exfoliated into ultrathin 2D MONs. Axially chiral diols such as 1,1'-binaphthol (binol) and 1,1′-biphenol are well established in the organic community as beneficial chiral auxiliaries for asymmetric catalysis and chiral recognition.[3,4] However, when diols are used as organocatalysts, they generally display low enantioselectivities.[4a] We describe here that both the 3D MOF bulk crystals and 2D MONs can be used as efficient catalysts for asymmetric cascade condensation and cyclization of anthranilamide and aromatic aldehydes and as fluorescent sensors for discriminating chiral amino alcohols. In both cases, the enantioselectivities increased in the order binol/biphenol < MOF bulk crystals < MONs, likely due to framework confinement effects and/or flexibility of the ultrathin framework layers with high surface utilization.

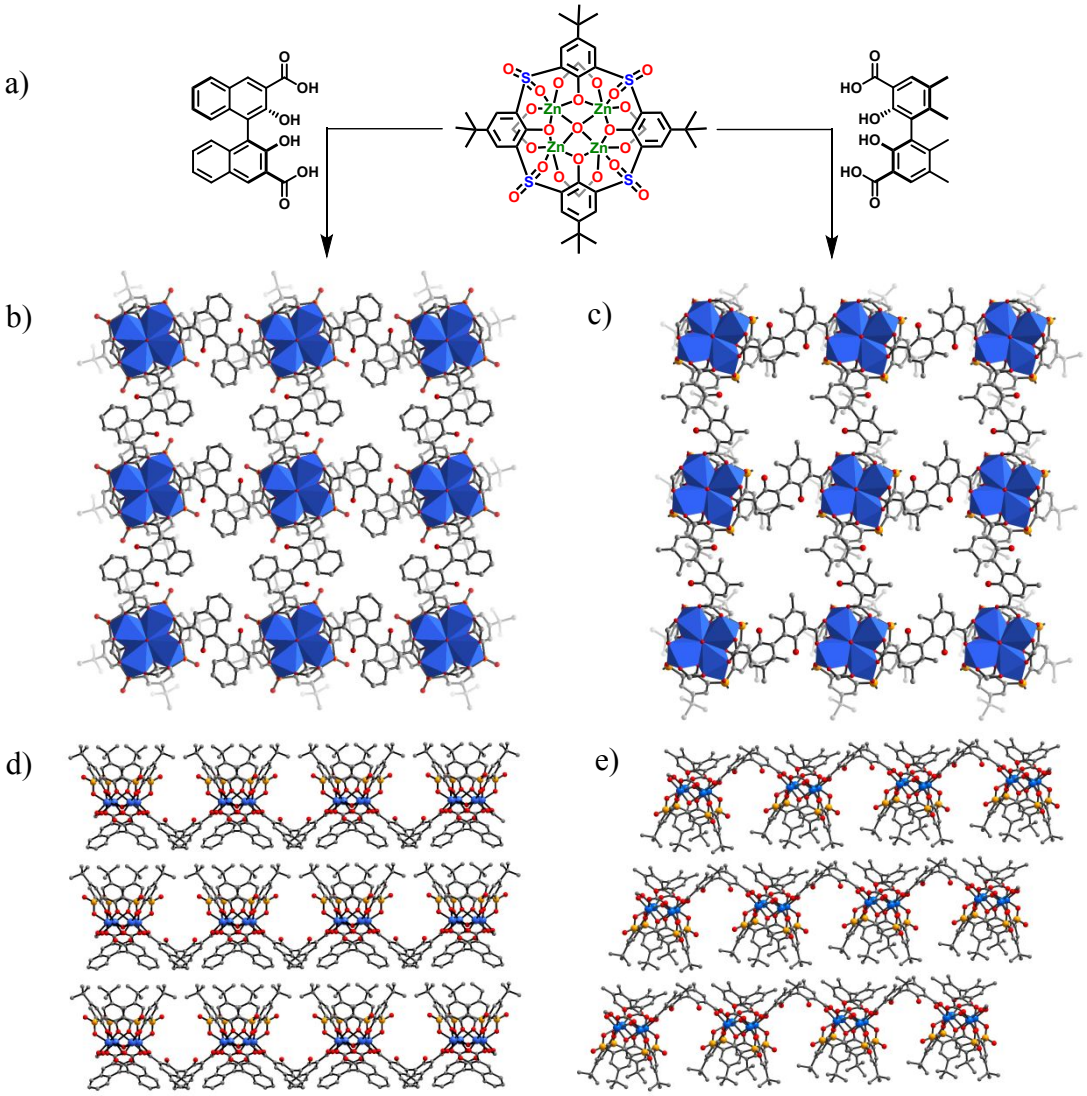

Figure 1. (a) Construction of MOFs **1** and **2** from H_2**L** and the Zn_4 cluster. (b, d) View of the 2D structure of MOF **1** along the *c*-axis and *b*-axis. (c, e) View of the 2D structure of MOF **2** along the *c*-axis and *b*-axis (Zn, blue; S, orange; O, red; C, grey).

RESULTS AND DISCUSSION

Synthesis and Characterization. The ligand $H_2\mathbf{L_1}$ was prepared from (*R*)- or (*S*)-2,2'-diethoxy-1,1′-binaphthalene in two steps in 80% overall yields, and $H_2\mathbf{L_2}$ was prepared from (*R*)- or (*S*)-5,5',6,6'-tetramethyl-3,3'-dibromo-1,1'-biphenyl-2,2'-diol in two steps in 39% overall yields. As shown in Figure 1, heating $Zn(NO_3)_2{\cdot}6H_2O$, H_4TBSC and $H_2\mathbf{L_1}$/$H_2\mathbf{L_2}$ in a mixed solvent of dimethylformamide (DMF) and CH_3OH or CH_3CN at 100 °C afforded colorless crystals of $[Zn_4(\mu_4\text{-}H_2O)(TBSC)][\mathbf{L_1}]_2{\cdot}3DMF{\cdot}CH_3OH{\cdot}6H_2O$ (**1**) and $[Zn_4(\mu_4\text{-}H_2O)(TBSC)][\mathbf{L_2}]_2{\cdot}DMF{\cdot}CH_3CN{\cdot}7H_2O$ (**2**). The products **1** and **2** have an average size of 38 and 48 μm, respectively (Figures 2b and S3). Both of them were stable in air and insoluble in water and common organic solvents. They were formulated based on single-crystal X-ray diffraction, IR spectra, elemental analysis and thermogravimetric analysis (TGA).

Single-crystal X-ray diffraction showed that MOF **1** crystallizes in the chiral space group *P*4, with one fourth of the formula in the asymmetric unit. As shown in Figure 1, in the shuttlecock-like $[Zn_4(\mu_4\text{-}H_2O)(TBSC)]$ cluster, each Zn ion is octahedrally coordinated by two phenoxo oxygen and one sulfonyl atom from

the deprotonated $TBSC^{4-}$ anion, one μ_4-H_2O atom and two carboxylate oxygen atoms from two $\mathbf{L_1}$ ligands. Each $\mathbf{L_1}$ ligand contains two bidentate carboxylate groups and the dihedral angle between the two binaphthyl subunits is 77.2°. Each Zn_4 cluster is linked by four exo-bidentate $\mathbf{L_1}$ ligands to four adjacent Zn_4 cores to give a 2D neutral framework in the *ab* plane, with the maximum thickness of 14.8 Å. A space-filling representation of MOF **1** (Figure S1d) clearly demonstrates the formation of chiral cavities.

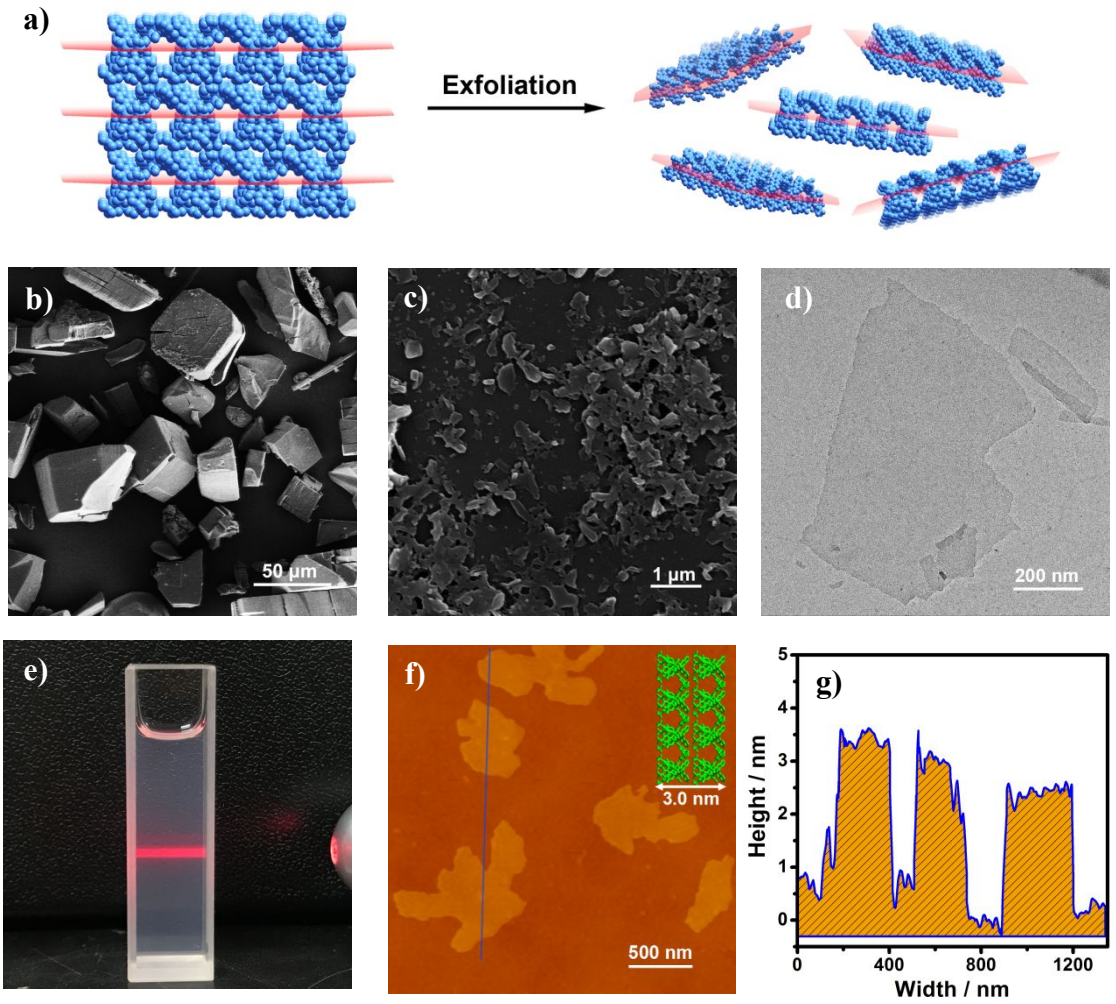

Figure 2. (a) Schematic diagram for the exfoliation of the bulk MOF **1** to ultrathin 2D nanosheets. **(**b) SEM image of MOF **1.** (c) SEM image of MON **1.** (d) TEM image of MON **1.** (e) The Tyndall effect of the MON **1** suspension in *i*-PrOH**.** (f) AFM image of MON **1.** (g) Height of AFM image for the selective area.

Interestingly, the hydroxyl groups of the BINOL point outwards the open cavities. Such 2D layers stack on each other along the *c*-axis, giving rise to 1D channels with a diameter of ~10.5 Å, in which hydroxyl groups point inwards and are accessible for guest molecules. The adjacent layers have weak van der Waals interactions between TBSC and $\mathbf{L_1}$ ligands. As shown in Figure 2b, the inherent layered structure can also be clearly seen from scanning electron microscopy (SEM) image.

MOF **2** crystallizes in the triclinic chiral space group *P*1, with the whole formula unit in the asymmetric unit. It has a very similar crystal structure to MOF **1**. Each shuttlecock-like [Zn_4(μ_4-H_2O)(TBSC)] cluster is quadruplely linked by four $\mathbf{L_2}$ ligands to afford a 2D layered structure (Figure 1e). The biphenol subunits of $\mathbf{L_2}$ have a similar dihedral angle to the binol of $\mathbf{L_1}$ (77.0° vs 77.2 °), and the maximum layer thickness decreases from 14.8 Å in **1** to 14.6 Å in **2** while the 1D channel size decrease from 10.5 Å to 10.0 Å (Figure S2). The adjacent layers are also linked by van der Waals interactions between TBSC and $\mathbf{L_2}$ ligands to form a porous framework with open channels that are periodically decorated with the dihydroxy groups of biphenyl backbones. Again, the layered structure can also be clearly revealed by scanning electron microscopy (SEM) image (Figure S3b).

Calculations using PLATON[19] show that MOFs **1** and **2** have about 43.1% and 42.9% void spaces, respectively, available for guest inclusion. Phase purity of the MOFs was established by comparison of their observed and simulated powder X-ray diffraction (PXRD) patterns (Figures 3a and 3b). Thermal gravimetric analysis (TGA) revealed that the MOFs started to decompose at about 350 °C (**1**) and 450 °C (**2**) (Figure S7). The permanent porosity was examined by CO_2 adsorption measurement at 195 K. The Brunauer-Emmett-Teller (BET) surface areas were calculated to be 175.9 and 141.1 m^2/g for MOFs **1** and **2**, respectively (Figures 3c and 3d). The enantiomeric nature of the MOFs was revealed by circular dichroism (CD) spectra. The *R*-/*S*-MOFs exhibited very strong bisignate $\pi - \pi^*$ bands at 256, 286, 306 and 361 nm for **1** and 254, 300 and 326 nm for **2**. The CD spectra were similar to those of the corresponding

enantiomers of ligands (251, 303 and 367 nm for $H_2\mathbf{L_1}$ and 262, 303 and 327 nm for $H_2\mathbf{L_2}$), indicating the cotton effects of MOFs derived from the chiral 1,1'-naphthyl or -phenyl skeletons. Moreover, the Cotton effects are much more intense in MOFs than in the ligands (Figure S6), indicating chiral amplification occurred during the framework crystallization. The ability to place such important chiral diol auxiliaries in layered MOFs represents a major step towards the controllable synthesis and structural tailoring of nanostructured porous materials.

Due to the weak van der Waals interactions between adjacent layers, these MOFs can be easily exfoliated into nanosheets through solvent-assisted liquid sonication (isopropanol for **1** and acetonitrile for **2**). The exfoliation can be evidenced by the Tyndall effect upon irradiation of the colloid suspensions of MONs with a laser beam (Figures 2e and S4). It shows the colloid suspensions remained stable at room temperature for at least six months, indicating the monodispersity of nanosheets. TEM and AFM analyses of the exfoliated MON **1** (Figure 2), and MON **2** (Figures S4 and S5) confirm their ultrathin 2D-nanosheet structural features. TEM images of MON **1** showed ultrathin and wrinkled nanosheets of 0.4 × 0.9 μm^2. AFM measurements gave a thickness of about 3 ± 0.5 nm for MON **1** (Figure 2g), which is about twice the theoretical thickness of monolayer (1.5 nm), indicating that MON **1** consists of double layers. In the same way, the size and thickness of MON **2** were evaluated as 1.0 × 0.5 μm^2 and (1.5~3.0) ± 0.5 nm (Figures S4c and S5b), respectively, indicative of a one- and two-layer nanosheets. More characterizations including FT-IR, CD and TGA also demonstrated the successful preparation of 2D nanosheets (Figures S6-S9). The BET surface areas were examined by CO_2 adsorption measurement at 195 K with 178.6 and 173.8 m^2/g for MON **1** and MON **2**, respectively (Figures 3c and 3d). This indicates both nanosheets can retain the porous structures as the pristine MOFs.

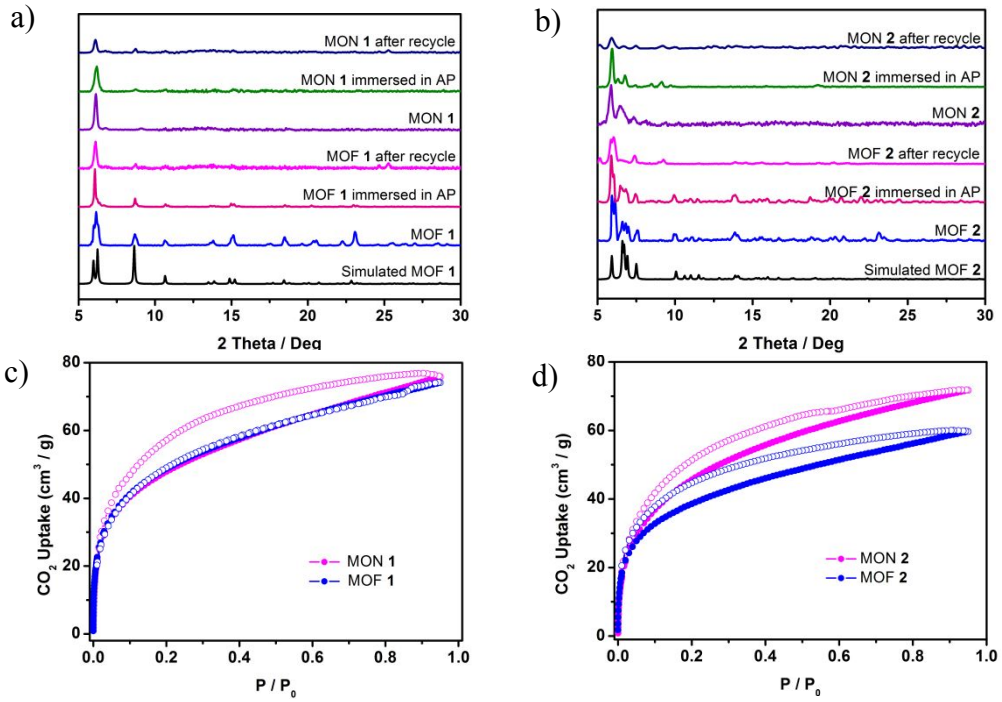

Figure 3. (a, b) PXRD patterns of the MOFs and MONs. (c, d) CO_2 adsorption (filled symbols) and desorption (open symbols) isotherms for the MOFs and MONs at 195 K.

Asymmetric Catalysis. The 2,3-dihydroquinazolinone (DHQZ) is a privileged scaffold for its extensive pharmacological activities such as antibacterial, antitumor, antifungal and analgesic efficacy.[20] Regardless of various methods that are available to synthesize DHQZs as racemates. Catalytic asymmetric synthesis of 2,3-DHQZ has been a challenge for a long time since the aminal stereocenter is sensitive to racemization. In fact, there are only several chiral Brønsted acids (BINOL- and SPINOL-phosphoric acids)[21,22] and Lewis acids (Sc(III)-inda -pybox)[23] that can catalyze condensation and cyclization of 2-aminobenzamide with aldehydes to produce enantiopure 2,3-DHQZ. Encouraged by the efficiency of Brønsted acids catalysts, the presence of potential hydroxyl protons active sites in the framework materials prompted us to evaluate their catalytic activities in condensation/amine addition cascade sequence to synthesize DHQZ.

To our delight, after screening various reaction conditions including catalyst loading, reaction time, solvent and temperature (Table S3), both MOFs and MONs were found to be active catalysts for condensation and cyclization of 2-aminobenzamide with aldehydes in CH_3CN at 40 °C. Specifically, 3.0 mol% loading of MOF or MON catalyzed the condensation/amine addition of 4-fluoro-benzaldehyde to give the targeted product in 91-94% yields and 72-92% ee in 60 h. As shown in Table 1, under the optimized conditions, other benzylaldehyde derivatives can also be transformed to the targeted DHQZ in 81~92% yields and 46~94% ee. In general, for a given catalyst, reaction of benzaldehydes bearing electron-withdrawing groups with 2-aminobenzamide afforded the DHQZ products in higher yields and ee values than the ones with electron-rich substituents. The absolute configuration of the product is determined by the handedness of the catalyst (entry 6 and 26). Despite the similar polymeric structures, MOF **1** and MON **1** showed much higher stereoselectivities in catalyzing the above reactions than MOF **2** and MON **2** (56-90% vs 46-72% ee and 72-94% vs 64-82% ee), respectively, probably arising from the bulky binol backbone of $\mathbf{L_1}$ has stronger enantioselective induction ability than the biphenol of $\mathbf{L_2}$. In addition, it appears that MONs **1** and **2** catalysts

gave improved reactivity and enantioselectivity related to the parent MOFs under similar conditions, as shown in Table 1 (entries 1-4 vs 6-9 and 21-24 vs 26-29). The differences in the reactivity and selectivity were clearly manifested in the reaction kinetics, as shown in Figures 4 and S12 (see below).

Table 1. Asymmetric condensation and cyclization of 2-aminobenzamide with aldehydes to synthesize DHQZs[a]

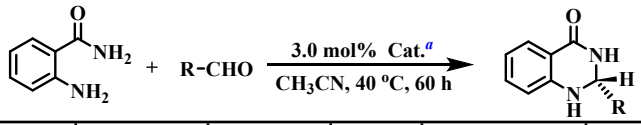

Entry	Cat.	R	Yield (%)[b]	ee (%)[c]	Entry	Cat.	R	Yield (%)[b]	ee (%)[c]
1	MOF **1**	4-FPh	91	88	21	MOF **2**	4-FPh	92	72
2		4-ClPh	85	90	22		4-ClPh	90	62
3		4-MeOPh	82	56	23		4-MeOPh	81	46
4		Ph	89	75	24		Ph	91	46
5		$G_1/G_2/G_3$[d]	99/39/~9	37/50/20	25		$G_1/G_2/G_3$	99/26/~2	20/11/20
6	MON **1**	4-FPh	92	92(-94)[g]	26	MON **2**	4-FPh	94	82 (-83)[g]
7		4-ClPh	90	94	27		4-ClPh	91	75
8		4-MeOPh	86	72	28		4-MeOPh	84	64
9		Ph	88	80	29		Ph	92	70
10		$G_1/G_2/G_3$	99/72/59	49/52/23	30		$G_1/G_2/G_3$	99/62/72	40/16/22
11	$Me_2\mathbf{L_1}$	4-FPh	93	0	31	$Me_2\mathbf{L_2}$	4-FPh	93	0
12		4-ClPh	88	0	32		4-ClPh	90	0
13		4-MeOPh	88	0	33		4-MeOPh	84	0
14		Ph	90	0	34		Ph	92	0
15		$G_1/G_2/G_3$	99/83/46	0/0/0	35		$G_1/G_2/G_3$	99/78/45	0/0/0
16	$H_2\mathbf{L_1}$	4-FPh	~99	0	36	$H_2\mathbf{L_2}$	4-FPh	~99	0
17	$H_2\mathbf{L_1}Me_2$[e]	4-FPh	98	0	37	$H_2\mathbf{L_2}Me_2$[e]	4-FPh	95	0
18	$H_2\mathbf{L_1}$+ **[Zn_4]**[f]	4-FPh	98	0	38	$H_2\mathbf{L_2}$+ **[Zn_4]**[f]	4-FPh	97	0
19	**[Zn_4]**	4-FPh	45	0	39	Spinol-P[h]	4-FPh	98	0
20	$Me_2\mathbf{L_1}$-**P**[i]	4-FPh	95	0	40	Binol-P[j]	4-FPh	97	0

[a] For reaction details see Experimental section. [b] Isolated yield. [c] The ee was determined by HPLC analysis. [d] G_1 = biphenyl, G_2 = 4-anthracylphenyl, G_3 = 3,5-bis(benzyloxy)phenyl; [e] The two phenolic hydroxyl groups of $H_2\mathbf{L}$ was protected by methyl groups . [f] A 2:1 mixture of tetramer with (*S*)-$Me_2\mathbf{L_1}$/-$Me_2\mathbf{L_2}$ (6.0 mol% loading) was used as a catalyst. [g] Catalyzed by the (*R*)-MON. [h](*R*)-1,1'-spirobiindane-7,7-diol-based spirocyclic phosphoric acid. [i]Phosphorylated $Me_2\mathbf{L_1}$ [j](*R*)-2,2'-diethoxy-1,1′-binaphthalene-based binol phosphoric acids

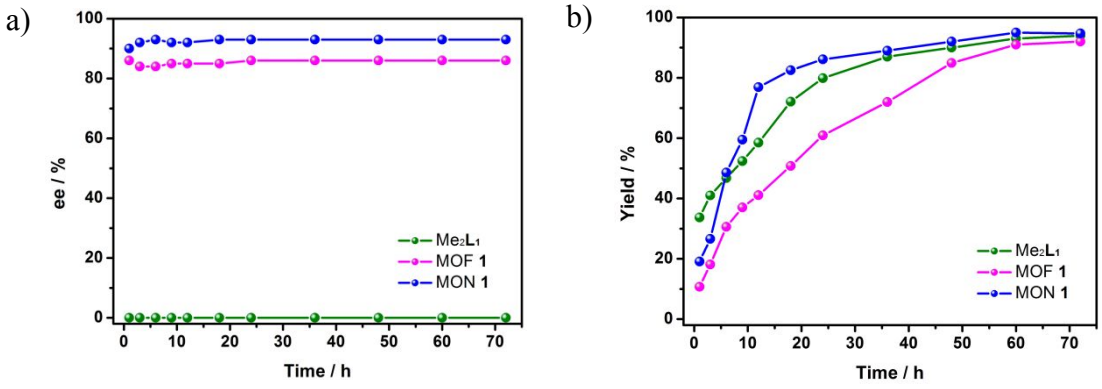

Figure 4. Plots of ee values (a) and yields (b) with 3.0 mol% MOF **1** and MON **1** and 6.0 mol% of $Me_2\mathbf{L_1}$ (the same loading of **L** as the heterogeneous reaction).

To understand the different catalytic performances of MOFs and their MONs, multiple control reactions were carried out. As shown in Table 1 (entries 16, 17, 36 and 37), with 3.0 mol% loading of $H_2\mathbf{L}$ or the ester $H_2\mathbf{L}Me_2$ (the same loading of **L** as the MOF catalyst), the reaction of anthranilamide with 4-fluoro-benzaldehyde proceeded smoothly, affording the product in more than 95% yield but with no enantioselectivity. The tetrameric cluster [$Zn_4(\mu_4$-$H_2O)$(TBSC)$(OAc)_4$] was also synthesized[18d] as a model complex of the Zn_4 building block in the MOF to catalyze the reaction, but only the racemic product was produced in 45% yield (Table 1, entry 19). Control reactions with a 2:1 mixture of the model Zn_4 complex and $H_2\mathbf{L}$ showed that they can promote the transformation smoothly (98% yield) but with no enantioselectivity (Table 1, entries 18 and 38). In contrast, as

mentioned above, the targeted DHQZ was produced in both high yield and enantioselectivity in the presence of catalytic amount of MOF **1** and MON **1**. Therefore, the above result showed that the **L** ligand and the Zn_4 cluster alone or their mixtures are incapable of providing efficient stereocontrol on the products. This indicates that the porous frameworks containing special chiral cavities made from **L** and $[Zn_4(\mu_4\text{-}H_2O)(TBSC)]$ is essential for enantioselective generation of chiral DHQZ.

The confinement effect was further demonstrated by the sharp contrast of catalytic activities of MON **1**, MOF **1** and $Me_2\mathbf{L_1}$ for condensation/amine addition cascade sequence at low catalyst/substrate (C/S) ratios (Table S6). At the C/S of 1:400, $Me_2\mathbf{L_1}$ afforded 83% conversion of the DHQZ, while MOF **1** and MON **1** gave 84 and 88% conversions, respectively. When the C/S ratio decreased from 1:400 to 1:1600 and 1:2400, the conversion dramatically decreased from 83 to 19 and 1% for $Me_2\mathbf{L_1}$, and from 84 to 60 and 14% for MOF **1**, whereas MON **1** could still achieve 69 and 41% conversions. So, the difference in catalytic activity became larger as the C/S ratio decreased, and it appeared in the order MON **1** > MOF **1** > $Me_2\mathbf{L_1}$. Similar catalytic performances were observed for $Me_2\mathbf{L_2}$ (3%), MOF **2** (14%) and MON **2** (46%) when the C/S ratios were decreased from 1:400 to 1:2400. The above finding further confirmed that the binol and biphenol units confined in the frameworks displayed much higher activity than the homogeneous counterparts, especially at low C/S ratio and also highlighted the key role of ultrathin nanosheet in improving catalytic performance.

We also monitored the dynamic process during the catalytic synthesis of 2-(4-fluorophenyl)-2,3-dihydroquinazolin-4(1*H*)-one by MONs, MOFs and $Me_2\mathbf{L}$, which exhibited quite different reaction kinetics. As seen from Figure 4a, the ee values of the DHQZ product experienced a period of 20 h to reach a stable value for MON **1** and MOF **1**, while they were always 0 for $Me_2\mathbf{L_1}$. Moreover, MON **1** gave higher enantioselectivity than MOF **1** in the whole reaction process. In terms of the kinetic profile of yield, the reaction rate with MON **1** is comparable with the homogeneous catalyst $Me_2\mathbf{L_1}$, but is obviously faster than MOF **1**, consistent with the fast diffusion of substrate and product within the ultrathin layers. Similar kinetic behaviors were observed for MON **2,** MOF **2** and $Me_2\mathbf{L_2}$ (Figure S12). These results further demonstrated the unique advantages of MONs. Upon completion of the catalytic reaction, both MONs and MOFs could be recovered by centrifugation and reused at least five times without any loss of its activity and enantioselectivity (Table S7). PXRD showed that both MOFs and MONs remained almost the same as the pristine samples after 5 catalytic recycles (Figures 3a and 3b). Moreover, filtration test showed no indication of catalysis by leached homogeneous species and inductively coupled plasma optical emission spectrometry (ICP-OES) analysis of the solution indicated almost no loss of Zn ions (0.005%) from the structure.

To probe the role of the pore aperture of MOFs and MONs in catalysis, several sterically aromatic aldehydes with size ranging from 10~16 Å were selected and subjected to the reactions. As expected, both $Me_2\mathbf{L_1}$ and $Me_2\mathbf{L_2}$ promoted homogeneous condensation and cyclization of 2-aminobenzamide with the bulky aldehyde**s** to produce DHQZ in high yields but with no enantioselectivity (Table 1, entries 15 and 35). MONs also showed highly efficient activity to the bulky substrates and in some cases even better than homogeneous catalysts. In contrast, the yields of the reaction products catalyzed by the MOFs greatly depend on the substituent size: as the size of the aldehyde increases, yields of the final products steadily decreases (99/39/9%, entry 5 and 99/26/2%, entry 25). Specially, only 9% yield of the product was detected for the sterically more demanding 3,5-bis(phenoxy-methyl) benzaldehyde catalyzed by MOF **1**, which was much lower than the 46% and 59% yields obtained with $Me_2\mathbf{L_1}$ and MON **1**, respectively, presumably because this aldehyde cannot access the catalytic sites in the channel (10.5 Å) as a result of its large diameters (10.2 × 16.0 $Å^2$). Besides, the ee values of the sterically products obtained with MON **1** were also higher than those with MOF **1**, as shown in Table 1 (entries 10 vs 5 and 30 vs 25), but the differences became smaller with the increase of the substrate diameters. It is thus likely that the catalytic asymmetric reactions may mainly occur within the MOFs and at the surfaces of MONs.

To provide microscopic insight into the high enantioselectivity of DHQZ in the synthesized MOFs and MONs, we performed DFT calculations for the reaction catalyzed by MON **1** (Figure S13). According to previous reports,[22, 23] the enantioselectivity of DHQZ is determined by the intramolecular amidation of imine. The attack of amine to the imine from the *Si* or *Re* face leads to (*S*)- or (*R*)-DHQZ. Thus, the intramolecular amidation of imine was chosen as the target reaction in our calculations. For comparison, the reactions with the homogeneous $Me_2\mathbf{L_1}$ catalyst and without catalyst were also examined.

The DFT calculations suggest that the intramolecular amidation of imine to DHQZ is a two-step process. In the first step, the nucleophilic attack of the N of amide group on imine C leads to a cyclization intermediate; in the second step, one H atom shifts from NH_2 to N to produce DHQZ. For the intramolecular amidation of imine to DHQZ without catalyst (Figure S14), the Gibbs energy profiles are exactly the same, implying the ee is 0.

In the homogeneous system with $Me_2\mathbf{L_1}$ catalyst, the reactant interacts with the hydroxyl groups through N-H and O-H hydrogen bonds (Figures S15 and S16), then it undergoes a two-step conversion from the *Si* and *Re* faces, respectively. To compare the enantioselectivity of DHQZ, the overall barrier (Gibbs energy difference between TS2/TS2' and A/A', Figure 5) is computed. For intramolecular amidation of imine on $Me_2\mathbf{L_1}$, the overall barriers are predicted to be 51.0 and 52.8 kcal/mol for (*S*)- and (*R*)-DHQZ, respectively, which give a small barrier difference of 1.8 kcal/mol.

In the heterogeneous system with MON **1** catalyst, the reactant interacts with the hydroxyl groups through N-H hydrogen bonds (Figures S17 and S18), and the 4-FPh group is located in the 1D chiral channel while another benzene ring points to the large cavity. The overall barriers for intramolecular amidation of imine to (*S*)- and (*R*)-DHQZ are 46.3 kcal/mol and 49.9 kcal/mol, respectively, which suggests (*S*)-DHQZ is more preferentially produced. The barrier difference of 3.6 kcal/mol for (*S*)- and (*R*)-DHQZ is higher than that (1.8 kcal/mol) on $Me_2\mathbf{L_1}$. This reveals MON **1** possesses higher enantioselectivity than $Me_2\mathbf{L_1}$, which is consistent with the experimentally observed trend. The intramolecular amidation of imine via *Si* face features less steric hindrance in the framework, which leads to the preferential production of (*S*)-DHQZ in MON **1** (Figures S17–S19).

Based on the above experimental studies, DFT calculations and literature findings,[21-24] the possible reaction pathway is proposed in Figure S20. The first imine formation step may be catalyzed by hydrogen-bonding between the hydroxyl group of the immobilized binol and the carbonyl group of aldehyde. The subsequent intramolecular amidation could be carried out by hydrogen-bonding between the hydroxyl group of binol and imino-group of the imino-amide intermediate to afford the final product. In the MOFs and their MONs, the 1D chiral channel lined with hydroxyl groups not only provides active protons to intrigue the condensation/amine addition cascade sequence, but also exerts specific stereocontrol over the intermediates by the confined chiral environment, which might offer 'enzyme-like' pockets available for stronger interactions between substrates and catalysts and thus better stereoselectivity. This behavior is, however, unavailable for the molecular catalyst $Me_2\mathbf{L}$ due to the lack of confinement effects, and reduced in the MOF catalysts owing to the limited flexibility and external surface areas. The

excellent stereoselective control of MONs may arise from specific interactions between substrate and ultrathin layers where the imino-amide intemediate diffuses into the chiral channel and gets access to chiral hydroxyl catalytic sites, while the two pendent aromatic form stable host-guest interactions with the binaphthyl/biphenyl skeletons of the ligand on the surfaces.

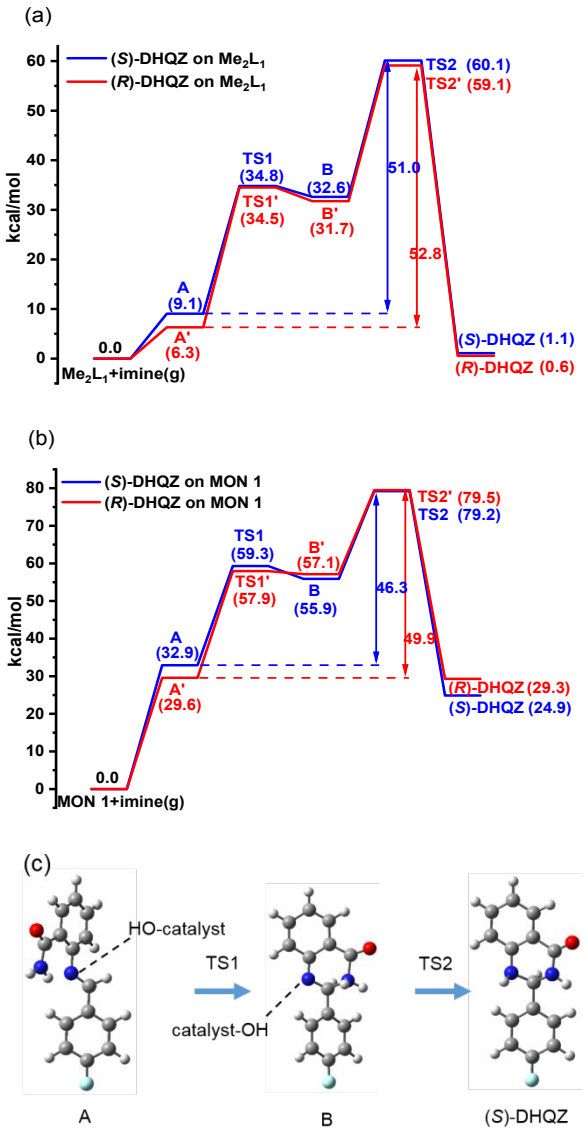

Figure 5. Relative Gibbs energy profiles at 313.15 K for the intramolecular amidation of imine to (*S*)- and (*R*)-DHQZ on (a) $Me_2\mathbf{L_1}$ and (b) MON **1**. (c) Schematic mechanism for (*S*)-DHQZ production on MON **1**. A/A': imine in adsorbed state; TS1/TS1': nucleophilic attack of the N of amide group on imine C; B/B': cyclization intermediate; TS2/TS2': H shift from NH_2 to N.

Although many heterogeneous asymmetric catalysts based on MOFs have been reported to display superior catalytic activity and selectivity to their homogenous analogues due to confinement effects,[9c,10b,11a] we demonstrate for the first time that the homogenous chiral catalyst can be boosted from completely non-selective to highly enantioselective when installed in MOF nanostructures. Despite great progresses in asymmetric organocatalysis,[3,21,22,25] there are no chiral diol catalysts reported for enantioselectively catalyzing acetalization reactions of 2-amino benzamide and aldehydes. The enantioselectivities of the present MON-based protocol are comparable even to those of the most enantioselective homogeneous systems based on phosphoric acids reported to date.[3b,22]

Enantioselective Sensing. The presence of chiral functional -OH groups in the present MOFs and MONs makes them good candidates for enantioselective recognition of chiral molecules. The MOF materials were tested for fluorescence enhancement by amino alcohols. Microcrystalline particles of MOFs **1** and **2** with an average size of 2.8 and 3.2 μm, respectively, were fabricated by vigorous stirring with a magnetic stir bar in acetonitrile (Figure S3). Both MOF particles and MONs show strong fluorescence in CH_3CN with emission maximum around 500 or 430 nm (Figure S10). They were dispersed in acetonitrile to prepare a stock solution with the binol/biphenol unit at a concentration of 10 μM. Aliquots containing different amounts of the *D* and *L* enantiomers of the amino alcohol were added to the acetonitrile suspensions (3 mL), and then the fluorescence signals of the suspensions in the presence of different amounts of substrates were measured. As shown in Figure 6c, when (*S*)-MON **1** was treated with 2-amino-1-propanol (alaninol), the emission at 430 nm was enhanced by both the *D* and *L* enantiomers, but the increase caused by *D*-alaninol was greater than that of *L*-alaninol, implying selectivity in the fluorescence recognition. The fluorescence intensity of MON **1** was maximally increased to 1.70 and 1.28 times that of the original value by *D*- and *L*-alaninol, respectively. Figure 6d shows Benesi-Hildebrand plots for MOF **1** and MON **1** (1.0×10^{-5} M) in the presence of *D*- or *L*-alaninol in CH_3CN. The association constants K_{BH} of MON **1** were calculated to be 2871.48 ± 143.19 M^{-1} with *D*-alaninol and 757.58 ± 48.75 M^{-1} with *L*-alaninol, giving an enantioselectivity (or enantiomeric resolution) factor [EF = $K_{BH(D\text{-alaninol})}/K_{BH(L\text{-alaninol})}$] of 3.79. MOF **1** was also enantioselective to alaninol with a $K_{BH(D)}/K_{BH(L)}$ value of 3.27, which was much smaller than that of MON **1**. Besides, other chiral amino alcohols such as leucinol, phenylalaminol and phenylglycinol can also enantioselectively enhance the fluorescence of MOF **1** and MON **1** (Figure S10). The $K_{BH(D)}/K_{BH(L)}$ values were determined to be 1.33, 1.43 and 1.86 for MOF **1** and 2.27, 1.54 and 2.17 for MON **1**, respectively.

From control experiment, the ester $Me_2\mathbf{L_1}$ of $H_2\mathbf{L_1}$ showed obvious low fluorescence enhancement and selectivity towards amino alcohols, with $K_{BH(D)}/K_{BH(L)}$ values ranging from 1.12 to 2.44. Therefore, for a given analyte, the enantioselectivity efficiency was in the order MON **1** > MOF **1** > $Me_2\mathbf{L_1}$. Although the $K_{BH(D)}/K_{BH(L)}$ values for these four amino alcohols are close for MOF **1** and $Me_2\mathbf{L_1}$, the fluorescence of the MOF is much more sensitive to the monomer enhancers. The observed change in the fluorescence intensity of the MOF material is probably caused by static enhancement via the formation of a hydrogen-bonded host-guest adduct that may perturb proton-transfer-assisted charge-transfer excited state. The static nature of the complexation is suggested by the consistent fluorescence lifetimes of the hosts before and after titration with alaninol (lifetime, τ_0, 1.60 vs 1.24 ns and 1.48 vs 1.07 ns, respectively). As the non-covalent interactions of the host with amino alcohol enantiomers afford different diastereomeric complexes, distinct fluorescence enhancement is thus observed. This finding is consistent with the catalytic result, as the MOFs and MONs confer a well-confined chiral environment for efficient enantiodiscrimination in comparison with $Me_2\mathbf{L}$ while the ultrathin nature of MONs facilitates better analyte diffusion and easier access to more exposed active sites.

Under otherwise identical conditions, MOF **2**, MON **2** and $Me_2\mathbf{L_2}$ also displayed enantioselectively binding with alaninol, leucinol, phenylalaminol and phenylglycinol (Figure S11). The $K_{BH(D)}/K_{BH(L)}$ values were determined as 1.72/3.30/1.43, 1.50/1.89/1.45, 1.50/1.80/1.11 and 1.72/2.14/1.31, respectively, and decreased in the order MON **2** > MOF **2** > $Me_2\mathbf{L_2}$, also proving the advantage of ultrathin nature of MONs in the

recognition of chiral analytes. Consistent with the slightly lower chiral induction ability of biphenol relative to binol, these enantioselective values are smaller than the related values for MOF **1**, MON **1** and Me_2**L**$_1$. Compared to the pristine samples, MOF **2** and MON **2** after titration exhibited slightly changes in fluorescence lifetimes (τ_0, 2.45 vs 2.44 ns and 1.69 vs 1.64 ns respectively), supporting the static nature of the host-guest complexation. In addition, PXRD indicated that all MOFs and MONs remained crystalline after treatment with *L*-alaninol, indicative of the good stability of the hosts **1** and **2** (Figures 3a and 3b). By taking advantages of the strong fluorescence of the BINOL core, a variety of enantiopure fluorescence sensors including organic oligomers, polymers and coordination assemblies have been prepared for chiral species with amino, hydroxyl and carboxylate groups that can generate hydrogen bonds with the binol hydroxyl groups.[26,27] Because of the ease of interfacing nanosheets with solid-state devices, the present chiral MON-based sensors hold the potential to perform online enantiomer discrimination, with perspectives in process monitoring.

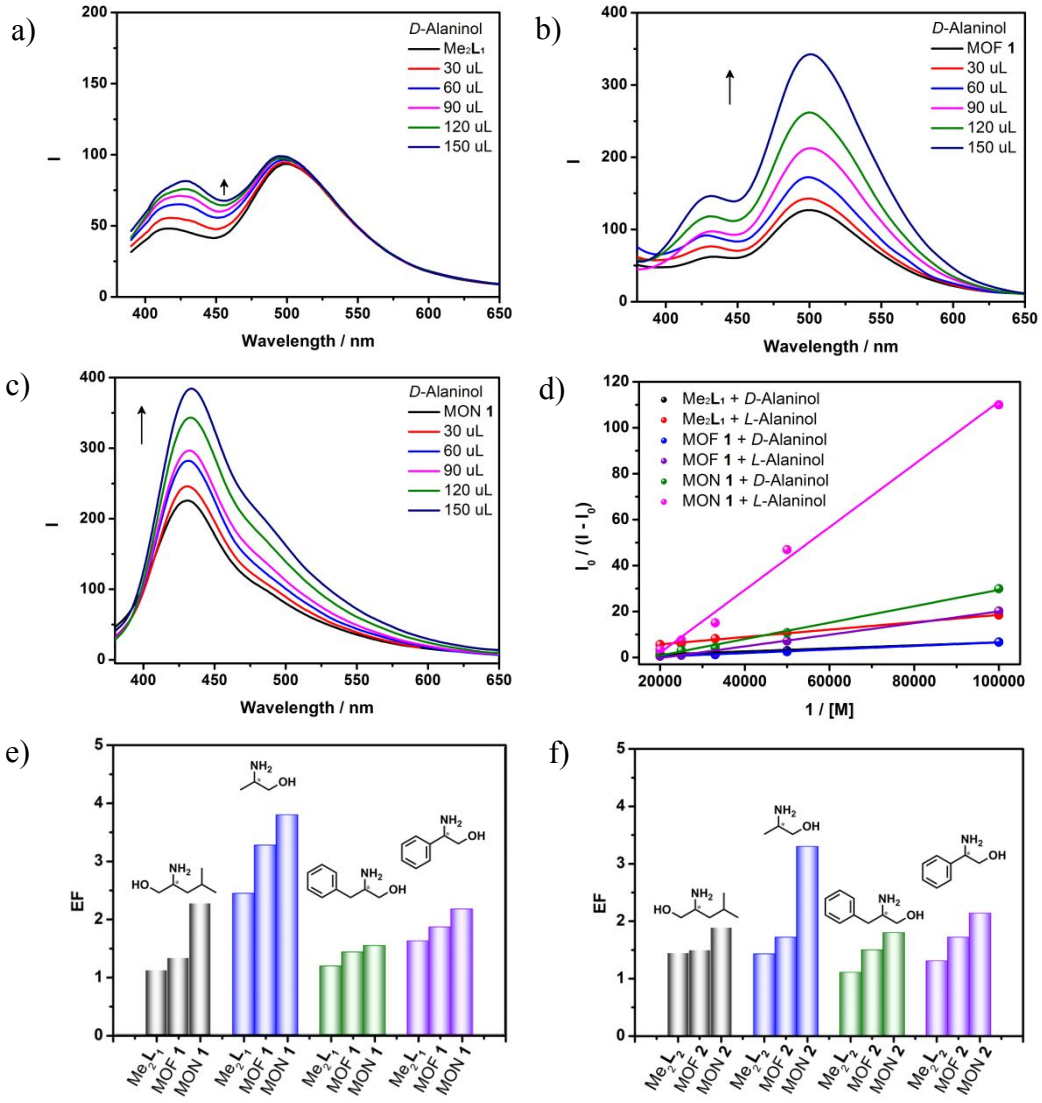

Figure 6. (a-c) Fluorescence emission spectra of (*S*)-Me_2**L**$_1$, MOF **1** and MON **1** with increasing concentrations of *D*-2-Alaninol in solutions. (d) Benesi-Hildebrand plots of the fluorescence emissions of Me_2**L**$_1$, MOF **1** and MON **1** enhanced by *D*-2- and *L*-2-Alaninol. (e,f) The comparative EFs of Me_2**L**, MOFs and MONs for four different amino alcohols.

CONCLUSIONS

We have shown that 3D layered porous MOFs and corresponding ultrathin 2D MONs can be synthesized from ligand-capped metal clusters and semi-rigid angular linkers. Controlled assembly of chiral binol/biphenol into MOF nanoparticles and nanosheets enabled the nonselective diol to enantioselectively catalyze condensation/amine addition cascade sequence to afford 2,3-dihyroquinazolinones with 56-90/46-72% ee and 72-94/64-82% ee, respectively. The MOF and MONs can also be sensitive fluorescent sensors for discriminating chiral amino alcohols and their enantioselectivity ratios were up to 1.4 and 2.3 times higher than those of the related diols. Therefore, the chiral diol catalysts can be boosted from completely non-selective to highly enantioselective when installed in MOF nanostructures, probably as a result of the steric hindrance and confinement effect of framework and/or 2D external surface of the flexible ultrathin layers. The nanostructured MOFs could be recycled and reused without a noticeable decrease in activity/sensitivity and selectivity. This

work thus provides a new strategy to induce and tailor stereoselectivity of organocatalyts and promises to develop a variety of 2D functional materials for enantioselective processes.

ASSOCIATED CONTENT

Supporting Information.
Experimental procedures, characterization data and DFT calculations. This material is available free of charge via the Internet at http://pubs.acs.org.

AUTHOR INFORMATION

Corresponding Author

*liuy@sjtu.edu.cn
*chejj@nus.edu.sg
*yongcui@sjtu.edu.cn

Notes
The authors declare no competing financial interest.

ACKNOWLEDGMENTS

This work was financially supported by the National Science Foundation of China (Grant Nos. 21431004, 21620102001, 21875136, and 91856204), the National Key Basic Research Program of China (2016YFA0203400), Key Project of Basic Research of Shanghai (17JC1403100 and 18JC1413200), and the Shanghai Rising-Star Program (19QA1404300).

REFERENCES

(1) (a) Arnum, P. V. Single-Enantiomer Drugs Drive Advances in Asymmetric Synthesis. *Pharm. Technol.* **2006**, *30*, 14. (b) Fumio, T. Enantiomer Separation: Fundamentals and Practical Methods. *Springer*, **2004**.
(2) Yoon, T. P.; Jacobsen, E. N. Privileged Chiral Catalysts. *Science* **2003**, *299*, 1691.
(3) (a) Mukherjee, J. W. Yang, S. Hoffmann, B. List. Asymmetric Enamine Catalysis. *Chem. Rev.* **2007**, *107*, 5471. (b) Parmar, D.; Sugiono, E.; Raja, S.; Rueping, M. Complete Field Guide to Asymmetric BINOL-Phosphate Derived Brønsted Acid and Metal Catalysis: History and Classification by Mode of Activation; Brønsted Acidity, Hydrogen Bonding, Ion Pairing, and Metal Phosphates. *Chem. Rev.* **2014**, *114*, 9047.
(4) (a) Gorin, D. J.; Sherry, B. D.; Toste, F. D. Modified BINOL Ligands in Asymmetric Catalysis. *Chem. Rev.* **2008**, *108*,3351. (b) Brunel, J. M. BINOL: A Versatile Chiral Reagent. *Chem. Rev.* **2005**, *105*, 857.
(5) (a) Blaser, H. U.; Schmidt, E. Asymmetric Catalysis on Industrial Scale: Challenges, Approaches and Solutions. *Angew. Chem. Int. Ed.* **2004**, *43*, 2600. (b) Wang, Z., Chen, G.; Ding, K. Self-supported Catalysts. *Chem. Rev.* **2009**, *109*, 322.
(6) (a) Furukawa, H.; Cordova, K. E.; O'Keeffe, M.; Yaghi, O. M. The Chemistry and Applications of Metal-Organic Frameworks. *Science* **2013**, *341*, 974. (b) Liu, Y.; Xuan, W.; Cui, Y. Engineering Homochiral MetalOrganic Frameworks for Heterogeneous Asymmetric Catalysis and Enantioselective Separation. *Adv. Mater.* **2010**, *22*, 4112. (c) Yoon, M.; Srirambalaji, R.; Kim, K. Homochiral Meta-Organic Frameworks for Asymmetric Heterogeneous Catalysis. *Chem. Rev.* **2012,** *112*, 1196.
(7) (a) Das, M. C.; Guo, Q.; He, Y.; Kim, J.; Zhao, C. G.; Hong, K.; Xiang, S.; Zhang, Z.; Thomas, K. M.; Krishna, R.; Chen, B. Interplay of Metalloligand and Organic Ligand to Tune Micropores within Isostructural Mixed-Metal Organic Frameworks (M'MOFs) for Their Highly Selective Separation of Chiral and Achiral Small Molecules. *J. Am. Chem. Soc.* **2012**, *134*, 8703. (b) Navarro-Sanchez, J.; Argente-Garcia, A. I.; Moliner-Martinez, Y.; Roca-Sanjuan, D.; Antypov, D.; Campins-Falco, P.; Rosseinsky, M. J.; Marti-Gastaldo, C. Peptide Metal-Organic Frameworks for Enantioselective Separation of Chiral Drugs. *J. Am. Chem. Soc.* **2017**, *139*, 4294. (c) Liu, B.; Shekhah, O.; Arslan, H. K.; Liu, J.; Woll, C.; Fischer, R. A. Enantiopure Metal-Organic Framework Thin Films: Oriented SURMOF Growth and Enantioselective Adsorption. *Angew. Chem. Int. Ed.* **2012**, *51*, 807. (d) Jeong, K. S.; Go, Y. B.; Shin, S.; Lee, S. M.; Kim, J.; Yaghi, O. M.; Jeong, N. Asymmetric Catalytic Reactions by NbO-Type Chiral Metal-Organic Frameworks. *Chem. Sci.* **2011**, 2, 877.
(8) (a) Seo, J. S.; Whang, D.; Lee, H.; Jun, S. I.; Oh, J.; Jeon, Y. J.; Kim, K. A Homochiral Metal-Organic Porous Material for Enantioselective Separation and Catalysis. *Nature* **2000**, *404*, 982. (b) Han, Q.; Qi, B.; Ren, W.; He, C.; Niu, J.; Duan, C. Polyoxometalate-Based Homochiral Metal-Organic Frameworks for Tandem Asymmetric Transformation of Cyclic Carbonates from Olefins. *Nat. Commun.* **2015**, *6*, 10007.(c) Liu, L.; Zhou, T. Y.; Telfer, S. G. Modulating the Performance of an Asymmetric Organocatalyst by Tuning Its Spatial Environment in a Metal–Organic Framework. *J. Am. Chem. Soc.* **2017**, 139, 39, 13936. (d) Gedrich, K.; Heitbaum, M.; Notzon, A.; Senkovska, I.; Froöhlich, R.; Getzschmann, J.; Mueller, U.; Glorius, F.; Kaskel, S. A Family of Chiral Metal-Organic Frameworks. *Chem. -Eur. J.* **2011**, *17*, 2099. (e) Tanaka, K.; Sakuragi, K.; Ozaki, H.; Takada, Y. Highly Enantioselective Friedel-Crafts Alkylation of N, N-dialkylanilines with Trans-*β*-nitrostyrene Catalyzed by a Homochiral Metal-OrganicFramework. *Chem. Commun*. **2018**, *54,* 6328. (f) Zhang, Z. X.; Ji, Y. R.; Wojtas, L.; Gao, W. Y.; Ma, S. Q.; Zaworotko, M. J.; Antilla, J. C. Two Homochiral Organocatalytic Metal Organic Materials with Nanoscopic Channels. *Chem. Commun*. **2013**, *49*, 7693.
(9) (a) Zheng, M.; Liu, Y.; Wang, C.; Liu, S.; Lin, W. Cavity-Induced Enantioselectivity Reversal in a Chiral Metal–Organic Framework Brønsted Acid Catalyst. *Chem*. Sci. **2012**, *3*, 2623. (b) Falkowski, J. M.; Sawano, T.; Zhang, T.; Tsun, G.; Chen, Y.; Lockard, J. V.; Lin W. Privileged Phosphine-Based Metal–Organic Frameworks for Broad-Scope Asymmetric Catalysis. *J. Am. Chem. Soc.* **2014**, 136, 5213. (c) Wu, C. D.; Hu, A.; Zhang, L.; Lin, W. A Homochiral Porous Metal-Organic Framework for Highly Enantioselective Heterogeneous Asymmetric Catalysis. *J. Am. Chem. Soc*. **2005**, *127*, 8940.
(10) (a) Mo, K.; Yang, Y.; Cui, Y. A Homochiral Metal-Organic Framework as an Effective Asymmetric Catalyst for Cyanohydrin Synthesis. *J. Am. Chem. Soc.* **2014**, *136*, 1746. (b) Chen, X.; Jiang, H.; Hou, B.; Gong, W.; Liu, Y.; Cui. Y. Boosting Chemical Stability, Catalytic Activity, and Enantioselectivity of Metal−Organic Frameworks for Batch and Flow Reactions. *J. Am. Chem. Soc.* **2017**, *139*, 13476. (c) Chen, X.; Peng, Y.; Han, X.; Liu, Y.; Lin, X.; Cui, Y. Sixteen Isostructural Phosphonate Metal-Organic Frameworks with Controlled Lewis Acidity and Chemical Stability for Asymmetric Catalysis. *Nat. Commun.* **2017**, *8*, 2171. (d) Peng, Y.; Gong, T.; Zhang, K.; Lin, X.; Liu, Y.; Jiang, J.; Cui, Y. Engineering Chiral Porous Metal-Organic Frameworks for Enantioselective Adsorption and Separation. *Nat. Commun.* **2014**, *5*, 4406.
(11) (a) Cho, S. H.; Ma, B.; Nguyen, S. T.; Hupp, J. T.; Albrecht-Schmitt, T. E. A Metal-Organic Framework Material that Functions as an Enantioselective Catalyst for Olefin Epoxidation. *Chem. Commun.* **2006**, 2563. (b) Zhu, C.; Yuan, G.; Chen, X.; Yang, Z.; Cui, Y. Chiral Nanoporous Metal-Metallosalen Frameworks for Hydrolytic Kinetic Resolution of Epoxides. *J. Am. Chem. Soc.* **2012**, *134*, 8058. (c) Xia, Q.; Li, Z.; Tan, C.; Liu, Y.; Gong, W.; Cui, Y. Multivariate Metal−Organic Frameworks as Multifunctional Heterogeneous Asymmetric Catalysts for Sequential Reactions. *J. Am. Chem. Soc.* **2017**, *139*, 24, 8259. (d), Song, F.; Wang, C.; Falkowski, J. M.; Ma, L.; Lin, W. Isoreticular Chiral Metal-Organic Frameworks for Asymmetric Alkene Epoxidation: Tuning Catalytic Activity by Controlling Framework Catenation and Varying Open Channel Sizes. *J. Am. Chem. Soc.* **2010**, *132*, 15390. (e) Falkowski, J. M.; Wang, C.; Liu, S.; Lin, W. Actuation of Asymmetric Cyclopropanation Catalysts: Reversible Single-Crystal to Single-Crystal Reduction of Metal–Organic Frameworks.*Angew. Chem. Int. Ed.* **2011**, *50*, 8674.
(12) (a) Makiura, R.; Motoyama, S.; Umemura, Y.; Yamanaka, H.; Sakata, O.; Kitagawa, H. Surface Nano-architecture of a Metal–Organic Framework. *Nat. Mater.* **2010**, *9*, 565. (b) Peng, Y.; Li, Y.; Ban, Y.; Jin, H.; Jiao, W.; Liu, X.; Yang, W. Metal-Organic Framework Nanosheets as Building Blocks for Molecular Sieving Membranes. *Science* **2014**, *346*, 1356. (c) Rodenas, T.; Luz, I.; Prieto, G.; Seoane, B.; Miro, H.; Corma, A.; Kapteijn, F.; Xamena, F. X. L.; Gascon, J. Metal–Organic Framework Nanosheets in Polymer Composite Materials for Gas Separation. *Nat. Mater.* **2015**, *14*, 48. (d) Liao, W. M.; Zhang, J. H.; Yin, S. Y.; Lin, H.; Zhang, X.; Wang, J.; Wang, H. P.; Wu, K.; Wang, Z.; Fan, Y. N.; Pan, M.; Su, C.Y. Tailoring Exciton and Excimer Emission in Exfoliated Ultrathin 2D-MOF. *Nat. Commun.* **2018**, *9*, 2401. (e) Metal−Organic Nanosheets Formed via Defect-Mediated Transformation of a Hafnium Metal−Organic Framework. Cliffe, M. J.;

Castillo-Martínez, E.; Wu, Y. ; Lee, J.; Forse, A. C.; Firth, F. C. N.; Moghadam, P. Z.; Fairen-Jimenez, D.; Gaultois, M. W.; Hill, J. A.; Magdysyuk, O. V.; Slater, B.; Goodwin, A. L.; Grey. C. P. *J. Am. Chem. Soc*. **2017**, *139*, 5397. (f) Zhao , M.; Huang, Y.; Peng, Y.; Huang, Z.; Ma, Q.; Zhang, H. Two-dimensional Metal–Organic Framework Nanosheets: Synthesis and Application. *Chem. Soc. Rev*., **2018**, 47, 6267.

(13) (a) Zhao, S.; Wang, Y.; Dong, J.; He, C. T.; Yin, H.; An, P.; Zhao, K.; Zhang, X.; Gao, C.; Zhang, L.; Lv, J.; Wang, J.; Zhang, J.; Khattak, A. M.; Khan, N. A.; Wei, Z.; Zhang, J.; Liu, S.; Zhao, H.; Tang, Z. Ultrathin Metal–Organic Framework Nanosheets for Electrocatalytic Oxygen Evolution. *Nat. Energy* **2016**, *1*, 1. (b) Cao, L.; Lin, Z.; Peng, F.; Wang, W.; Huang, R.; Wang, C.; Yan, J.; Liang, J.; Zhang, Z.; Zhang, T.; Long, L.; Sun, J.; Lin, W. Self-Supporting Metal–Organic Layers as Single-Site Solid Catalysts. *Angew. Chem. Int. Ed.* **2016**, *55*, 4962. (c) Li, F. L.; Wang, P.; Huang, X.; Young, D. J.; Wang, H. F.; Braunstein, P.; Lang, J. P. Large-Scale, Bottom-Up Synthesis of Binary Metal–Organic Framework Nanosheets for Efficient Water Oxidation. *Angew. Chem. Int. Ed.* **2019**, *58*, 7051.

(14) (a) Zhao, M.; Wang, Ma, Y. Q.; Huang, Y.; Zhang, X.; Ping J.; Zhang, Z.; Lu, Q.; Yu, Y.; Xu, H.; Zhao, Y.; Zhang, H. Ultrathin 2D Metal–Organic Framework Nanosheets. *Adv. Mater.* **2015**, *27*, 7372. (b) Foster, J. A.; Henke, S.; Schneemann, A.; Fischercd, R. A.; Cheetham, A. K. Liquid Exfoliation of Alkyl-ether Functionalised Layered Metal–Organic Frameworks to Nanosheets. *Chem. Commun.* **2016**, *52*, 10474.

(15) Guo, J.; Zhang, Y.; Zhu, Y.; Long, C.; Zhao, M.; He, M.; Zhang, X.; Lv, J.; Han, B.; Tang, Z. Ultrathin Chiral Metal-Organic Framework Nanosheets for Efficient Enantioselective Separation. *Angew. Chem. Int. Ed.* **2018**, *57*, 6873.

(16) (a) Au, V. K. M.; Nakayashiki, K.; Huang, H.; Suginome, S.; Sato, H.; Aida, T. Stepwise Expansion of Layered Metal−Organic Frameworks for Nonstochastic Exfoliation into Porous Nanosheets. *J. Am. Chem. Soc.* **2019**, *141*, 53. (b) Ding, Y.; Chen, Y. P.; Zhang, X.; Chen, L.; Dong, Z.; Jiang, H. L.; Xu, H.; Zhou, H. C. Controlled Intercalation and Chemical Exfoliation of Layered Metal-Organic Frameworks Using a Chemically Labile Intercalating Agent. *J. Am. Chem. Soc.* **2017**, *139*, 9136. (c) Huang, J.; Li, Y.; Huang, R. K.; He, C. T.; Gong, L.; Hu, Q.; Wang, L.; Xu, Y. T.; Tian, X. Y.; Liu, S. Y.; Ye, Z. M.; Wang, F.; Zhou, D. D.; Zhang, W. X.; Zhang, J. P. Electrochemical Exfoliation of Pillared-Layer Metal-Organic Framework to Boost the Oxygen Evolution Reaction. *Angew. Chem. Int. Ed.* **2018**, *57*, 4632.

(17) W. J. Roth, Barbara Gil, W. Makowski, B. Marszalek, P. Eliášová. Layer Like Porous Materials with Hierarchical Structure. *Chem. Soc. Rev.,* **2016**,*45*, 3400.

(18) (a) Hang, X.; Liu, B.; Zhu, X.; Wang, S.; Han, H. Liao, W.; Liu, Y. Hu, C. Discrete $\{Ni_{40}\}$ Coordination Cage: A Calixarene-Based Johnson-Type (J_{17}) Hexadecahedron, *J. Am. Chem. Soc.* **2016**, 138, *9*, 2969. (b) Qiao, Y.; Zhang, L,; Li, J.; Lin, W.; Wang, Z. Switching on Supramolecular Catalysis via Cavity Mediation and Electrostatic Regulation. *Angew. Chem. Int. Ed.* **2016**, *55*, 12778. (c) Fang, Y.; Xiao, Z.; Li, J.; Lollar, C. Liu, L.; Lian, X. Yuan, S. Banerjee, S. Zhang, P.; Zhou. H. C. Formation of a Highly Reactive Cobalt Nanocluster Crystal within a Highly Negatively Charged Porous Coordination Cage. *Angew. Chem. Int. Ed.* **2018**, *57*, 5283. (d) Tan, C.; Jiao, J.; Li, Z.; Liu, Y.; Han, X. and Cui. Y. Design and Assembly of a Chiral Metallosalen-Based Octahedral Coordination Cage for Supramolecular Asymmetric Catalysis. *Angew. Chem. Int. Ed.* **2018**, *57*, 2085.

(19) Spek, A. Single-Crystal Structure Validation with the Program PLATON. *J. Appl. Crystallogr.* **2003**, *36*, 7.

(20) (a) Chinigo, G. M.; Paige, M.; Grindrod, S.; Hamel, E.; Dakshanamurthy, S.; Chruszcz, M.; Minor, W.; Brown, M. L. Asymmetric Synthesis of 2,3-dihydro-2-arylquinazolin-4-ones: Methodology and Application to a Potent Fluorescent Tubulin Inhibitor with Anticancer Activity. *J. Med. Chem.* **2008**, *51*, 4620. (b) Xu, Z.; Zhang, Y.; Fu, H.; Zhong, H.; Hong, K.; Zhu, W. Antifungal Quinazolinones from Marine-Derived Bacillus Cereus and their Preparation. *Bioorg. Med. Chem. Lett.* **2011**, *21*, 4005.

(21) (a) Cheng, X.; Vellalath, S.; Goddard, R.; List, B. Direct Catalytic Asymmetric Synthesis of Cyclic Aminals from Aldehydes. *J. Am. Chem. Soc.* **2008**, *130*, 15786. (b) Cheng, D. J.; Tian, Y.; Tian, S. K. Catalytic Asymmetric Synthesis of Dihydroquinazolinones from Imines and 2-Aminobenzamides. *Adv. Synth. Catal.* **2012**, *354*, 995.

(22) (a) Huang, D.; Li, X.; Xu, F.; Li, L.; Lin, X. Highly Enantioselective Synthesis of Dihydroquinazolinones Catalyzed by SPINOL-Phosphoric Acids. *ACS Catal.* **2013**, *3*, 2244. (b) Kausar, N.; Roy, I.; Chattopadhyay, D. and Das, A. R. Synthesis of 2,3-dihydroquinazolinones and Quinazolin-4(*3H*)-ones Catalyzed by Graphene Oxide Nanosheets in an Aqueous Medium: "on-Water" Synthesis Accompanied by Carbocatalysis and Selective C-C Bond Cleavage. *RSC Adv.* **2016**, *6*, 22320.

(23) Prakash, M. and Kesavan, V. Highly Enantioselective Synthesis of 2,3-Dihydroquinazolinones through Intramolecular Amidation of Imines. *Org. Lett.*, **2012**, *14*, 1896.

(24) Lou, S.; Moquist, P. N.; Schau, S. E. Asymmetric Allylboration of Ketones Catalyzed by Chiral Diols. *J. Am. Chem. Soc*. **2006**, *128*, 12660.

(25) Gong, W.; Chen, X.; Jiang, H.; Chu, D.; Cui, Y. ; Liu, Y. Highly Stable Zr(IV)-Based Metal-Organic Frameworks with Chiral Phosphoric Acids for Catalytic Asymmetric Tandem Reactions. *J. Am. Chem. Soc.* **2019**, *141*, 7498.

(26) (a) Pu, L. 1,1'-Binaphthyl Dimers, Oligomers, and Polymers: Molecular Recognition, Asymmetric Catalysis, and New Materials. *Chem. Rev.* **1998**, *98*, 2405. (b) Pu, L. Enantioselective Fluorescent Sensors: A Tale of BINOL. *Acc. Chem. Res.* **2012**, 45, 150.

(27) (a) Wanderley, M. M.; Wang, C.; Wu, C. D.; Lin, W. A Chiral Porous Metal-Organic Framework for Highly Sensitive and Enantioselective Fluorescence Sensing of Amino Alcohols. *J. Am. Chem. Soc.* **2012**, *134*, 9050. (b) Wu, X.; Han, X.; Xu, Q. Liu, Y.; Yuan, C.; Yang, S.; Liu, Y.; Jiang, J.; Cui, Y. Chiral BINOL-Based Covalent Organic Frameworks for Enantioselective Sensing. *J. Am. Chem. Soc.* **2019**, *141*, 7081.

Graphic Content